


ARTICLE

Open Access

Magnetic–acoustic biphysical invisible coats for underwater objects

Yi Zhou¹, Jian Chen^{2,3}, Liu Liu⁴, Zheng Fan³ and Yungui Ma¹ 

Abstract

Magnetic fields and acoustic waves are the two fundamental measures to perceive underwater objects, which, however, have never been simultaneously handled before. In this work, we propose and demonstrate a biphysical submillimeter-thick metamaterial coat that can simultaneously make underwater objects invisible to both magnetic fields and acoustic waves. The conformal coat is a subtle integration of an open-cavity acoustic absorber made of a dissipative acoustic metasurface (AMS) and a bilayer magnetic cloak. Experimentally, a magnetic cloaking effect with a field disturbance ratio of <math><0.5\%</math> is obtained over a broad-frequency range (10–250 kHz), and the compound metamaterial coat can strongly attenuate ultrasonic waves with a near-unity absorptivity. The magnetic subcoat can be freely combined with various AMS layers to achieve a wideband acoustic stealth effect for different spectral regimes. This work may open up a new way to build multifunctional devices for various waterborne applications.

Introduction

Invisible cloaking is one of the representative advancements of modern electromagnetics research associated with the development of metamaterials^{1–5}. To date, various techniques have been developed to improve the feasibility of electromagnetic (EM) cloaking devices^{6–10}. The same conception has also been broadly extended to other physical systems controlled by different partial differential equations^{11–14}. However, from the perspective of practice, it is still a rather challenging task to implement a cloaking device for EM or other waves, primarily limited by the complexity of material fabrication. Fortunately, the difficulty will be greatly reduced when we consider low-frequency applications where electric and magnetic fields are effectively uncoupled. In 2012, Gömöry et al. demonstrated a direct current (d.c.) magnetic cloak using

a superconductor–ferromagnetic (SC–FM) bilayer structure under the application of the static Laplace equation¹⁵. Later, different groups largely developed this technique, extending it to the quasi-static regime, so that magnetic cloaks could work at room temperature without a SC for both static and dynamic frequencies^{16–20}. Potential applications may be broadly envisioned, as magnetic fields are widely involved in various technologies and instruments. One of the possible scenarios is for waterborne applications, where generally, magnetic fields and acoustic waves are regarded as the two fundamental measures to deliver signals or perceive objects. While acoustic cloaks have also been similarly proposed using coordinate transformation^{21,22}, it is very hard to implement this kind of inhomogeneous anisotropic device. Great efforts by engineering either anisotropic mass density^{23–27} or, more recently, anisotropic modulus²⁸, have been made to prove this novel acoustic function. Even complex devices made of mechanical pentamode metamaterials have been built for elastic waves whose equation does not satisfy the general coordinate transformation invariance²⁹. Like the EM counterpart, however, these advanced acoustic devices are still far from practice when considering their structure complexity, thickness, and bandwidth. However,

Correspondence: Yungui Ma (yungui@zju.edu.cn)

¹State Key Lab of Modern Optical Instrumentation, Centre for Optical and Electromagnetic Research, College of Optical Science and Engineering, International Research Center for Advanced Photonics, Zhejiang University, 310058 Hangzhou, China

²State Key Lab of Fluid Power and Mechatronics Systems, School of Mechanical Engineering, Zhejiang University, 310027 Hangzhou, China

Full list of author information is available at the end of the article.

These authors contributed equally: Yi Zhou, Jian Chen.

© The Author(s) 2020



Open Access This article is licensed under a Creative Commons Attribution 4.0 International License, which permits use, sharing, adaptation, distribution and reproduction in any medium or format, as long as you give appropriate credit to the original author(s) and the source, provide a link to the Creative Commons license, and indicate if changes were made. The images or other third party material in this article are included in the article's Creative Commons license, unless indicated otherwise in a credit line to the material. If material is not included in the article's Creative Commons license and your intended use is not permitted by statutory regulation or exceeds the permitted use, you will need to obtain permission directly from the copyright holder. To view a copy of this license, visit <http://creativecommons.org/licenses/by/4.0/>.

in practice, a thin absorber is equally important and highly desired for stealth technology based on the measurement of returning loss³⁰. This consideration is valid for a far-field, single-station wave characterization system, but not suitable for a near-field system, including the magnetic field probe. There are some works about dual-physics metasurfaces that can manipulate electromagnetic and acoustic waves simultaneously^{31,32}. However, magnetic–acoustic biphysical invisible coats for underwater objects have not been explored before.

In this work, we propose and demonstrate a biphysical metamaterial invisible coat that can simultaneously deal with the detection of both magnetic field and acoustic waves for underwater objects. For this purpose, the magnetic invisible cloak and the acoustic stealth functional structure are compatibly merged together within a single compact design. Returning to the early idea of circuit analog absorbers (CAAs) for EM waves^{33,34}, we design an ultrathin acoustic impedance-matched broadband absorber (Fig. 1) consisting of a resonant AMS, a sound spacing layer, and a rigid bottom ground, with a deep discussion on the absorption characteristics that were not fully uncovered before^{35–37}. One of our major contributions is to design a high-permeability elastic FM spacing layer so that its combination with the inner rigid metallic ground can give rise to a desired bilayer magnetic invisible cloaking effect. It is also revealed that when the FM and AMS layers are thin enough, i.e., transparent for

each other in their specific responses, their relative positions in the compound metamaterial can be alternated, which offers more freedom to build biphysical coats for different wave bands. These expectations have been well confirmed from the experimental measurements. The ultrathin bifunctional protecting coat developed here may find key applications not only for military purposes but also for civilian uses, for example, as partially evidenced, to control the magnetic and ultrasonic disturbances of implanted metallic objects in medical scanning.

Materials and methods

Simulation for the magnetic cloak

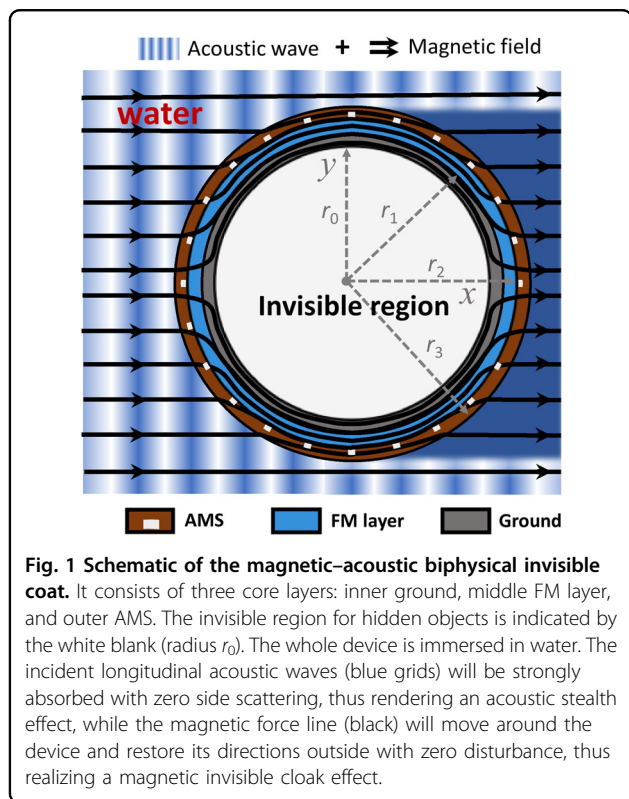
The commercial software COMSOL MULTIPHYSICS 5.4 is used to optimize and calculate the magnetic field scattered by the bilayer magnetic cloak. In the simulations, we chose the 2D model to simulate the response of the infinite bilayer cylinder. The electric conductivity of the brass (C28000) ground layer with a radius r_1 of 11 mm was set as 1.62×10^7 S. The relative permeability of the ferromagnetic layer with a thickness t_{FM} ($t_{FM} = r_2 - r_1$) was set as $(\mu_{rr}, \mu_{\theta\theta}, \mu_{zz})$ in the cylindrical system, where $\mu_{rr} = 1$ and $\mu_{\theta\theta} = \mu_{zz} = \mu$. We utilized COMSOL with the MATLAB module to optimize the permeability μ_{FM} for different t_{FM} values (relative to the radius ratio $r_2/r_1 = 1 + d/r_1$) with the initial starting point calculated by the theoretical solution for the condition with the ideal superconductor ground shell $\mu_{FM} = (r_2^2 + r_1^2)/(r_2^2 - r_1^2)$ ¹⁵. The object function was defined as

$$o(\mu_{FM}; t_{FM}) = |\eta_H(\mu_{FM}; t_2, f = 250 \text{ kHz}) - (-0.005)|$$

Here, we try to optimize μ_{FM} to minimize the difference between the relative change at 250 kHz (which is the upper measure limit of our lock-in amplifier) and -0.5% , which will extend the working bandwidth of the cloak as broadly as possible.

Simulation for the acoustic absorber

Considering the working band of our acoustic measurement system, we optimized the center frequency of the acoustic absorber to ~ 100 kHz (the actual value is 105 kHz). The diameter D , height H , and period p of the air cylinder holes are 0.15, 0.15, and 2.3 mm, respectively. To prevent the air holes from being filled by the water, another thin PDMS layer was added below the bubble metasurface. Here, the distance between the air matrix and the upper boundary of the PDMS $h = 255 \mu\text{m}$. The thickness of the whole PDMS $t_1 = 1.05$ mm. In the acoustic simulations, the thickness of the FM layer is fixed at $t_{FM} = 0.13$ mm. With this small t_{FM} , we find that the existence of the FM layer is marginal to the acoustic response with varying density and mechanical properties. The Acoustic-Solid Interaction and Frequency Domain



modules in COMSOL MULTIPHYSICS were used to simulate the acoustic absorber. The plane-wave radiation boundary condition was used in the water, and the low-reflecting boundary condition was used in the brass to mimic an infinite extended space with Floquet periodic side boundaries. The parameters of the PDMS were set according to ref. ³⁵ (density $\rho = 970 \text{ kg/m}^3$, shear modulus $\mu = 0.6 + 0.7f \text{ MPa}$ with the acoustic frequency f in MHz, and impedance $Z = 1 \text{ MRayl}$). We utilized water, liquid, and UNS C28000 in the Material Library of COMSOL to simulate the water and brass, where the Poisson ratio of the brass was set as 0.362.

Sample fabrication

The magnetic cloak is first fabricated by rolling a 0.13-mm-thick soft magnetic sheet around a brass (C28000) cylinder with a diameter of 22 mm and length of 50 mm. The FM sheet is a mixture composed of the PDMS matrix randomly embedded with plate-shaped hydroxyl iron nanoparticles. The flat iron nanoparticles are aligned by a bias magnetic field during the solidification of PDMS to achieve a large in-plane permeability. The volume ratio is a variable used to tune the permeability of the composite. To obtain the qualitative permeability value, we roll the film into a cigarette-shaped core (diameter 5 mm and length 34 mm). A pair of Helmholtz coils (diameter 33 cm, spacing 11 cm, and turns 30) driven by the internal oscillator of a lock-in amplifier (Signal Recovery 7270, AMETEK Inc., Santiago, CA, USA) is built. The axis component of the oscillating magnetic field in the center of the Helmholtz coils is inductively measured by a ring prober (diameter 9 mm) made of 16-turn copper wire loops connected to the lock-in amplifier at 1–250 kHz. The permeability spectrum is obtained from the comparison of the induced complex signals with and without the FM core. The acoustic absorber is successively realized by covering the magnetic coat with a soft AMS. An SU-8 mold has been used to make the AMS with a standard UV lithography process. First, the photoresist SU-8 2075 is spin-coated at a rotation speed of 1600 rpm for 30 s on a 4-inch silicon wafer and baked at 65 °C for 5 min and 95 °C for 30 min on a hot plate. Then, the resist is exposed to UV light and baked at 65 °C for 5 min and 95 °C for 12 min. Finally, propylene glycol methyl ether acetone (PGMEA) is used as the developer. An ultrasonic agitator is used to increase the developing speed. The thickness of the SU-8 structure is determined by a profiler. The diameter and period of the posts are measured by a microscope. The PDMS polymer (SYLGARD 184 Silicone Elastomer Base and Curing Agent mixed with a 10:1 mass ratio, Dow Corning Corp., Midland, MI, USA) is placed in the vacuum-drying oven for 2 h for debubbling. Then, the mixture is directly poured on the SU-8 mold and allowed to stand for 5 min in air to form a thick

PDMS film (~1 mm). Next, the film is baked at 85 °C for 20 min and peeled off the mold. Then, we fabricate another thin PDMS film to encapsulate the thick PDMS film. The upper layer of PDMS is spin-coated on a 4-inch silicon wafer to form an ~50- μm -thick PDMS film (spin-coated at 1000 rpm for 1 min). Next, the film is baked at 85 °C for 10 min. The preprocessed thick PDMS film is bonded with the upper PDMS layer. Then, the whole part is baked at 85 °C for 1.5 h and peeled off the wafer. During the experiment, water may enter the gap between the AMS and the FM layer, which will help to reduce the boundary acoustic reflection.

Measurement for magnetic cloaking

To evaluate the performance of the device, we adopt the relative change of the measured voltage $\eta_V = \frac{|V_S| - |V_0|}{|V_0|}$, where $|V_S|$ and $|V_0|$ are the measured voltages with and without the sample, respectively. To perform the experiment, we prepare a pair of Helmholtz coils (diameter = 33 cm and height = 1.8 cm) sourced by a signal generator (Stanford DS345, Stanford Research Systems Inc., Sunnyvale, CA, USA) and immerse them in a water tank ($50 \times 50 \times 20 \text{ cm}^3$) (Fig. 4c). The local field is scanned by a small Helmholtz coil connected to the lock-in amplifier, which is driven by a programmed step motor. In the second experiment, we use a commercial handheld metal scanner (Tianxun 1001B, Tianxun Electronic Equipment Co., Ltd., Shanghai, China) to examine the actual performance of the magnetic cloak at an operating frequency of 25 kHz. The alarm (“beep” sound and flash) will be triggered if the scanner perceives a metallic object. The induced signal is output using an oscilloscope (Agilent DSO1022A, Agilent Technologies, Inc., Santa Clara, CA, USA).

Measurement for acoustic stealth

The water immersion experiments are carried out in reflection mode, and the setup consists of a transducer, a pulser, and a digital storage oscilloscope. A round PZT transducer (Panametrics V1011, Olympus Scientific Solutions Americas Inc., Waltham, MA, USA) with a central frequency of 100 kHz is used as shown in Fig. 5a–c to generate the normally incident plane wave, and is placed at a distance of 150 mm from the sample to operate in the far field. In the experiment, a ten-cycle Hann-windowed tone-burst signal at 100 kHz is generated with an output voltage of 300 V and a repetition frequency of 25 Hz. To measure the response, as shown in Fig. 6c, another PZT transducer (VA1C11325, Doppler Electronic Technologies Co., Ltd., Guangzhou, China) with a central frequency of 1 MHz is used, which is fed by a pulse signal with a central frequency of 1 MHz and a –6-dB bandwidth of 0.4 MHz at an output voltage of 150 V and a pulse repetition of 100 Hz. The pulser (RAM-5000, Ritec Inc.,

Warwick, RI, USA) is responsible for the emission of the ultrasonic signals to excite the transducer. The ultrasonic waves reflected from the sample are then received by the same transducer and routed to the digital oscilloscope (Lecroy HDO6054, Teledyne Technologies Inc., Thousand Oaks, CA, USA) for AD conversion via a diplexer (RDX-6, Ritec Inc., Warwick, RI, USA). RDX-6 is a broadband (0.25–45 MHz) passive device that separates the high-voltage emission signal and low-voltage ultrasonic signal. The time-trace signals are sampled with a sampling frequency of 10 MHz and averaged 500 times to improve the signal-to-noise ratio. These signals are stored in the oscilloscope and sent to a PC for further analysis. From the time-domain signals, we obtain the reflection spectrum via Fourier transform. The reflectivity is the result of dividing the signals with and without the metamaterial coat.

Results

Sample design and simulation

For the simplicity of implementation, we choose a two-dimensional (2D) bifunctional structure with a cylindrical invisible inner cavity (see Fig. 1). The overall principle of the same discussions could be applied to the three-dimensional (3D) case as well^{18,19}. For practical purposes, the composite coat should be flexible, and the thickness should be controlled to be as small as possible. To meet these requirements, as mentioned above, we adopt a multilayer stacking design to manipulate both acoustic waves (i.e., CAA³⁵) and magnetic fields (i.e., bilayer coat¹⁵), which are subtly merged together according to their working algorithms. In previous works^{19,20}, we have shown that the combination of an FM layer and a diamagnetic metallic (screening) core could give rise to a dynamic magnetic cloaking effect. As shown in Fig. 2a, this bilayer magnetic cloak can work in a broad-frequency range from a few to hundreds of kilohertz, depending on the conductivity σ of the metal used¹⁹ and the choice of permeability μ_{FM} for the FM shell. Here, the relative change η_{H} is defined by the change ratio of the local magnetic field with (H_{s}) and without (H_0) a sample, i.e., $\eta_{\text{H}} = (|H_{\text{s}}| - |H_0|)/|H_0|$, and a magnetic cloaking behavior is claimed if $|\eta_{\text{H}}| < 0.5\%$ (the shaded region in Fig. 2a). At lower frequencies, such as $f < 1$ kHz, the ohmic loss will greatly increase and degrade the desired diamagnetic property of the metal shell. This problem may be compensated by an active current boundary, as we showed quite recently²⁰. As a purely passive approach, this type of bilayer cloak will have lower and upper cutoff frequencies f_{L} and f_{U} , respectively. In principle, f_{U} could be designed to be orders of magnitude larger than f_{L} . In this work, f_{U} is fixed at 250 kHz in order to match the maximum measurement frequency of our lock-in amplifier. In our biphysical hiding coat design, according to the algorithm,

a smaller thickness t_{FM} for the FM layer is highly desired. Physically, the bilayer structure with an ultrathin FM layer could help to reduce all the terms of the magnetic response higher than the dipole³⁸. A thin FM layer is also a prerequisite for the compact design of acoustic components. Figure 2b shows that the desired permeability for the FM layer swiftly increases as its thickness becomes a fractional number of the inner metallic core. For example, at $r_1 = 11$ mm and $r_2 = 1.012 r_1 = 11.13$ mm (i.e., $t_{\text{FM}} = 0.13$ mm), the theoretical μ_{FM} is 85.25 according to the formula $\mu_{\text{FM}} = (r_2^2 + r_1^2)/(r_2^2 - r_1^2)$ ¹⁵. From zero to radio frequencies, such large values are available, for example, using soft ferrite or Fe-based particle–polymer composites. Note that the analytical permeability is derived on the assumption of a perfectly conductive metallic core, and in reality, it needs to be modified, such as by using a numerical method¹⁹. As shown in Fig. 2b, the modification is obvious at a small t_{FM} where the bandwidth is increased accordingly. Figure 2c depicts one snapshot of the simulated field response of a magnetic cloak sample with a total bilayer thickness of 0.63 mm at 25 kHz. There is nearly no disturbance for the external field, while a large hiding cavity with almost zero magnetic field is obtained inside. The ratio of the sample thickness to the radius of the cloaking region is 0.06, a value hardly achievable by any wave cloak^{3,25,39}. Such a thin magnetic component is vital for the successive design of the acoustic absorber. The skin depth associated with the eddy current loss plays a decisive role in the operating band. The dynamic magnetic field profile (see Supplementary Movie 1) shows that the sample would cloak all phases of the a.c. cycle of the magnetic field. As shown in Fig. 2d, the upper bound f_{U} or bandwidth will drop dramatically when the inner metallic shell is thinner than 0.5 mm, which thus becomes a boundary value for the device design. The curve also indicates that a thicker inner shell will not help much to reduce the lower-frequency bound f_{L} due to the ohmic loss.

The acoustic stealth property, as shown in Fig. 3a, is achieved initially by stacking an AMS on top of the magnetic cloak. The AMS is made of a layer of air bubbles in the soft polydimethylsiloxane (PDMS) (density $\rho = 970$ kg/m³, shear modulus $\mu = 0.6 + 0.7f$ MPa with the acoustic frequency f in MHz, and impedance $Z = 1$ MRayl^{35,40}). The bubble cavities will exhibit Minnaert resonance at angular frequencies $\omega_0 = \sqrt{(3\beta_{\text{g}} + 4\mu)/\rho/a}$, where β_{g} is the bulk modulus of the air and a is the radius of the bubble^{39,41}. The resonant AMS will lead to a high-impedance-like π -phase shift for the reflected wave, which will balance out the other portion with a 0-phase shift directly reflected back from the rigid brass ground below, thus mimicking a classic EM circuit analogy absorber³³. Note that in the mechanical simulation, the FM layer has

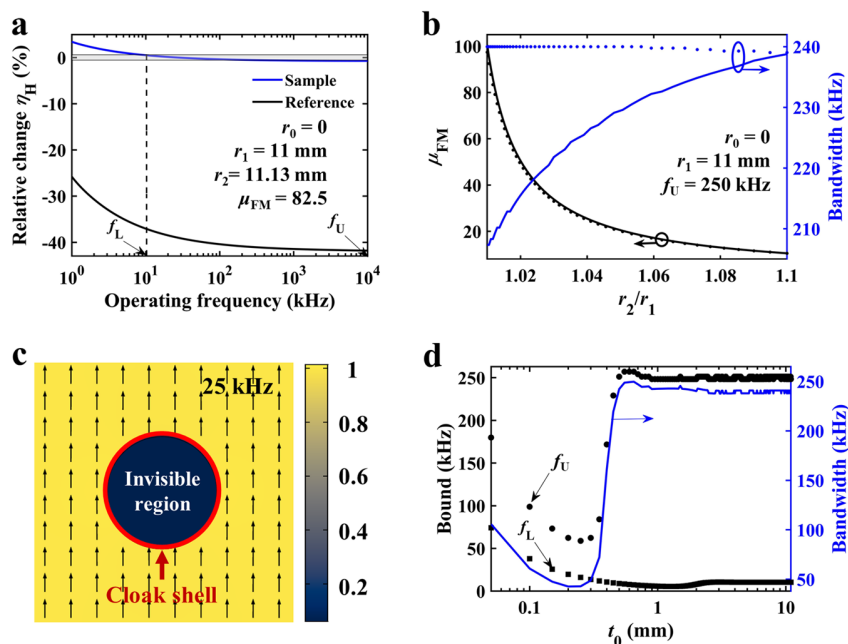


Fig. 2 Design of the magnetic cloak. **a** The relative change η_H of the magnetic field as a function of frequency for the sample with $r_0 = 0$, $r_1 = 11$ mm, $r_2 = 11.13$ mm, and $\mu_{FM} = 82.5$ at $(0, r_3 + 6$ mm). The shaded gray area corresponds to the region where $|\eta_H| < 0.5\%$, which is defined by a lower (f_L) and an upper (f_U) boundary frequency. **b** The desired permeability for the FM layer (thickness $t_{FM} = r_2 - r_1$) and the bandwidth as a function of the ratio r_2/r_1 with a fixed upper bound frequency $f_U = 250$ kHz. The solid lines are analytically calculated, and the symbols denote numerically optimized results. **c** The simulated magnetic field at one phase moment for the sample with the parameters $r_0 = 10.5$ mm, $r_1 = 11$ mm, $r_2/r_1 = 1.01_2$, and $\mu_{FM} = 82.5$ at 25 kHz. The arrows represent the direction of local magnetic fields, and the amplitude is denoted by the colors. **d** The dependences of bound frequencies and bandwidth on the thickness t_0 of the inner metal shell.

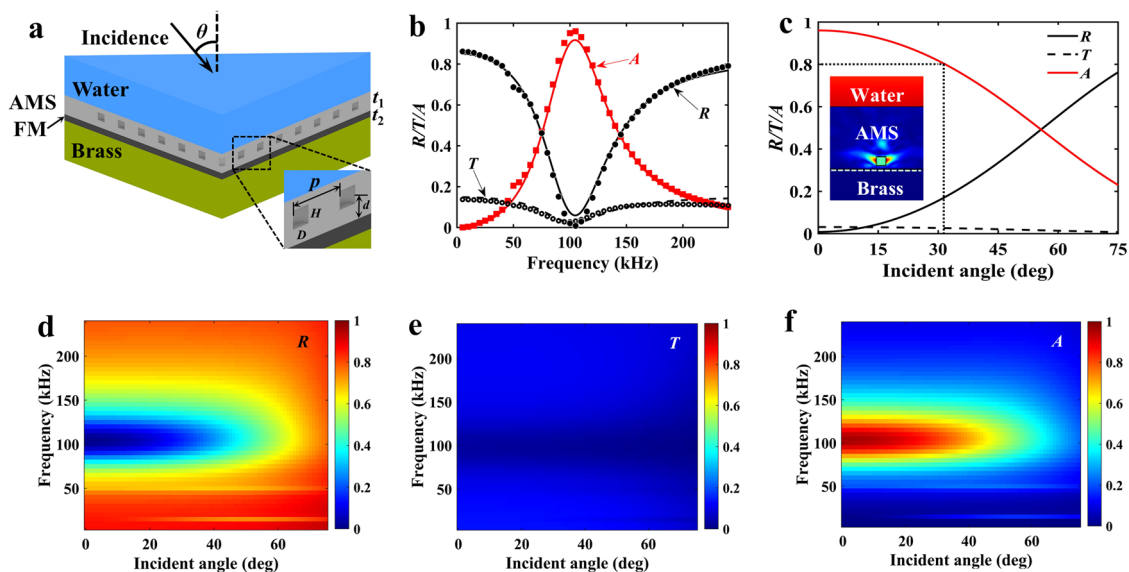


Fig. 3 Design of the acoustic absorber. **a** Schematic of the biphysical invisible coat design. From top to bottom, it consists of an AMS layer, FM layer, and rigid brass ground layer. The AMS layer is made of a PDMS elastic sheet periodically doped with air-hole cavities. **b** The reflectivity (R), transmissivity (T), and absorptivity (A) spectra of an optimized absorber with parameters $D = H = 150$ μ m, $p = 2.3$ mm, $d = 255$ μ m, and $t_1 = 1.05$ mm. The solid lines denote the analytical results, and the symbols denote the simulation results. The inset draws the acoustic displacement in PDMS, and pressure in water and air cavity patterns at normal incidence. **c** The same scattering parameters for the sample as a function of the incident angle at 100 kHz. **d-f** The angle- and frequency-dependent scattering parameters R , T , and A for the same sample.

been assumed to be one part of the acoustic spacer as in the experiment, so we will use the PDMS matrix with Fe-particle inclusions to fabricate it. The calculations indicate that a moderate change in its mechanical parameters will slightly affect the acoustic absorption performance due to the small thickness ($t_{\text{FM}} < 0.2$ mm). In the absorber, viscosity will be the primary dissipative damping factor for our absorber. The distance between the air bubbles will be a key factor in tuning the near-field coupling and the absorptivity. This type of absorber can be made thin and broadband. Although brass in water used here is not an ideal rigid ground as is the case in air, it can still be regarded as a good reflector^{35,42}, in particular compared with the PDMS and FM layers, which have an impedance similar to that with water. The existence of the submillimeter-thick FM layer will only slightly affect the resonance and then the absorption characteristics of the acoustic absorber at our first frequencies of interest of ~ 100 kHz (14.8 mm in wavelength). Figure 3b plots the numerical reflectivity (R), transmissivity (T), and absorptivity (A) curves of a sample under normal longitudinal wave incidence. Here, $R + T + A = 1$. The parameters for the cylindrical air cavities are height $H = 150$ μm , diameter $D = 150$ μm , period $p = 2.3$ mm, and distance to the ground $d = 255$ μm . The numerical computation by the finite-element method is very time consuming due to the excitation of shear waves and the near-field coupling among the bubbles. For an AMS made of bubbles with a near-unity aspect ratio H/D in a soft elastomer ($\mu < 10$ MPa), Leroy et al. previously found that a semi-analytical formula could be used to describe its scattering properties by approximating a spherical cavity with diameter $a = (3D^2H/16)^{1/3}$ ^{39,43}. Here, we found that a revision factor of 1.13 for D would make the approximation nearly perfect in order to match the analytical results (dotted lines) with the simulated results (solid lines). The details are addressed in the “Materials and methods” section. As shown in Fig. 3b, a strong absorption peak with $A = 0.96$ is achieved at ~ 100 kHz, and the bandwidth with $A > 80\%$ is ~ 30 kHz. Figure 3c plots the scattering coefficients as a function of the incident angle θ for the same sample at 100 kHz, which indicates good absorption up to 32° . This absorber can protect metallic objects from the detection of a general single-station measurement system. The angular performance is primarily determined by the coupling efficiency (inversely proportional to θ) of the incident wave with the elastic resonance mode, as shown in the inset of Fig. 3c, which has a symmetric displacement distribution along the normal irrespective of θ . The scattering properties at various frequencies are depicted in Fig. 3d–f. Similarly, the dynamic pressure field and displacement profiles (see Supplementary Movie 2) indicate that the sample would absorb all phases of the a.c. cycle of the acoustic wave. It is clear that the designed

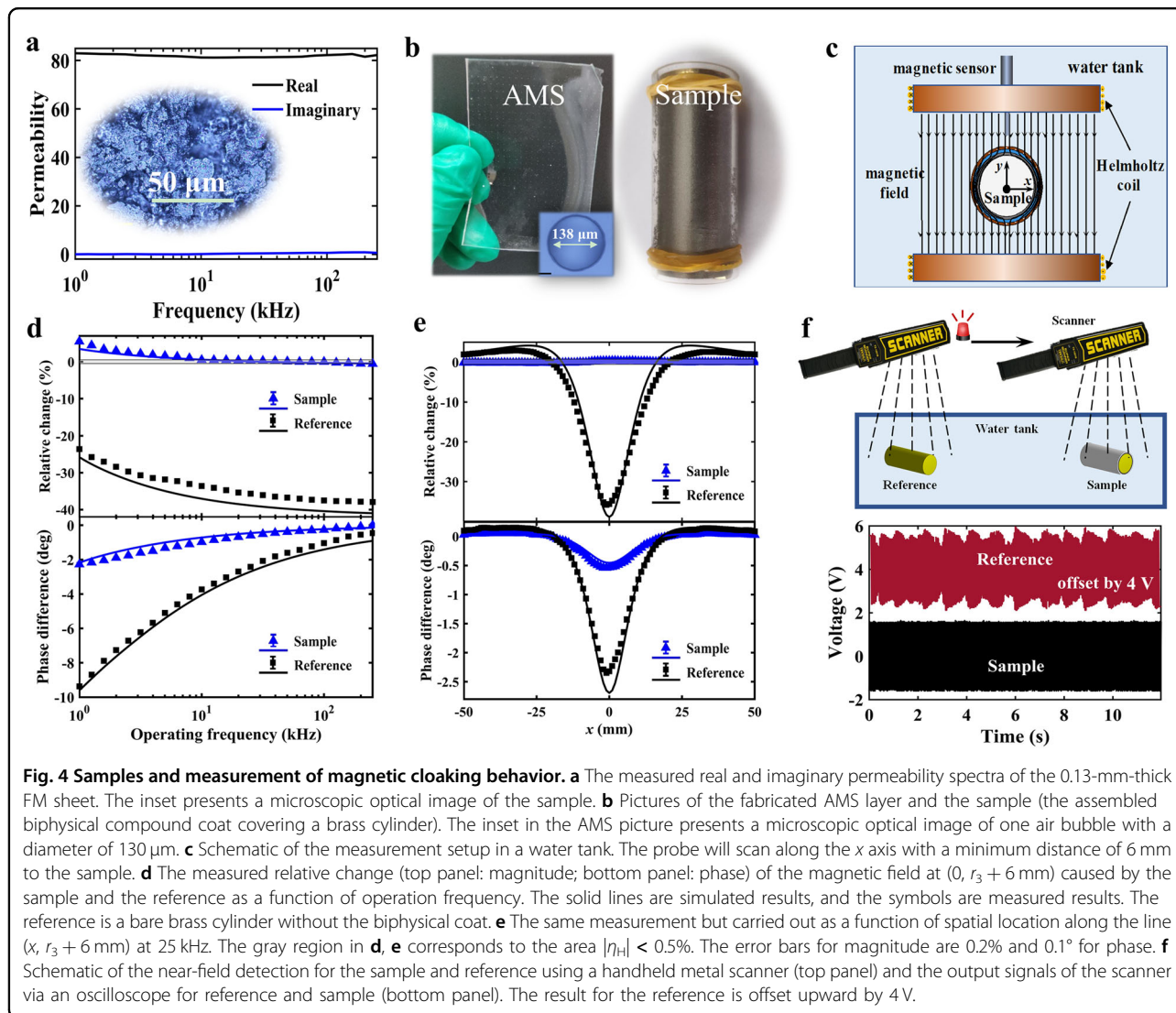
absorber has certain broadband and wide-angle response capabilities. The transmittance is rather small. As we shall discuss later, the bandwidth can be further enhanced by introducing multiple resonance modes. To demonstrate this concept, we will implement a simple structure with a single-sized cavity.

Sample fabrication

The sample includes magnetic and acoustic parts, which are separately manufactured and merged together later. To have an ultrasmall thickness, the FM layer should possess very large permeability while remaining insulating and mechanically soft. To meet these requirements, we use plate-shaped hydroxyl iron nanoparticles as magnetic inclusions, and mix them with PDMS in a mold. The composite is solidified in a magnetic field in order to align the particles and maximize the in-plane permeability. The magnetic properties can be optimized by tuning the volume ratio of the particle inclusions to the matrix. From the in-plane and out-of-plane hysteresis loops (see Supplementary Fig. S1a), we see that the fabricated FM sheet has a large magnetic anisotropy with small coercivities (\sim few Oerster). Figure 4a shows the real and imaginary permeability spectra of the fabricated FM sheet measured by an induction method using a Helmholtz coil circuit and a lock-in amplifier (see Supplementary Fig. S1b). The real permeability is ~ 82 from 0 to 250 kHz, and the imaginary part is close to zero. The inset gives a microscopic optical picture of the FM sheet, indicating the clustering of flat flakes, and thus explains the high-permeability values. The measured resistivity is above 10^6 Ω cm. With this FM composite, we design a bilayer magnetic cloak with $t_{\text{FM}} = 0.13$ mm and $r_1 = 11$ mm. The biphysical invisible coat (Fig. 4b) is then realized by covering the magnetic cloak with a submillimeter-thick AMS made of air-holed PDMS. The inset in the AMS picture gives a microscopic optical image of one cylindrical air bubble. The fabrication process is described in the Materials and methods section.

Magnetic measurement

The magnetic cloaking effect is then characterized in a pair of custom-made Helmholtz coils that are placed in a water tank (Fig. 4c). Figure 4d shows the measured amplitude and phase disturbances of the magnetic field of the sample (FM sheet-covered brass cylinder) and the reference (naked brass cylinder) at a fixed near point (0 , $r_3 + 6$ mm). The measured results (symbols) are in good agreement with the numerical predictions (solid lines). Our sample exhibits good magnetic cloaking behavior from 10 to 200 kHz, where $|\eta_{\text{H}}| < 0.5\%$, and the phase variation is $< 1^\circ$. Figure 4e shows the amplitude and phase disturbances scanned along the line parallel to the x axis at $y = r_3 + 6$ mm at 25 kHz. Different from the strong



signals induced by the reference, our sample gives rise to much weaker disturbances to the probing field. Here, using a 0.13-mm-thick FM coat, the maximum field disturbance ratio of a 22-mm-thick brass cylinder is greatly suppressed by more than two orders of magnitude and five times in phase. To expose the practical potential, we use a common handheld commercial metal scanner to check the EM response of these two samples, which are placed inside a water tank (Fig. 4f). The reference will trigger the alarm with a “beep” sound, while the bilayer coat could apparently trick the prober without sounding an alarm when scanned at a close distance (see Supplementary Movie 3). Connecting the output of the prober to an oscilloscope, we can clearly see the difference of the induced signals when it scans over the reference (upper) and the sample (lower) (Fig. 4f). Therefore, the magnetic cloaking performance and its practical potential are experimentally verified by our ultrathin bilayer coat.

Acoustic measurement

The acoustic stealth measurement setup (Fig. 5a) is described in detail in the Materials and methods section. Here, we examine the acoustic stealth property of two samples, i.e., the compound metamaterial sheets covering a brass plate (Sample 1) and the compound metamaterial sheets covering a brass cylinder (Sample 2). As shown in Fig. 5a, the acoustic experiment is conducted in a water tank and operated in reflection mode with an ultrasonic system, which consists of a transducer, a pulser, and a digital storage oscilloscope under the control of a computer. The nominal central frequency of the transducer is 100 kHz, and therefore, the distance between the transducer and sample is set to 150 mm to ensure a far-field measurement. The ultrasonic waves reflected from both the sample (R^S) and the tank wall (R^W) are recorded. As shown in Fig. 5b, the acoustic absorber can greatly reduce the reflection of the ultrasonic wave from a rigid plate

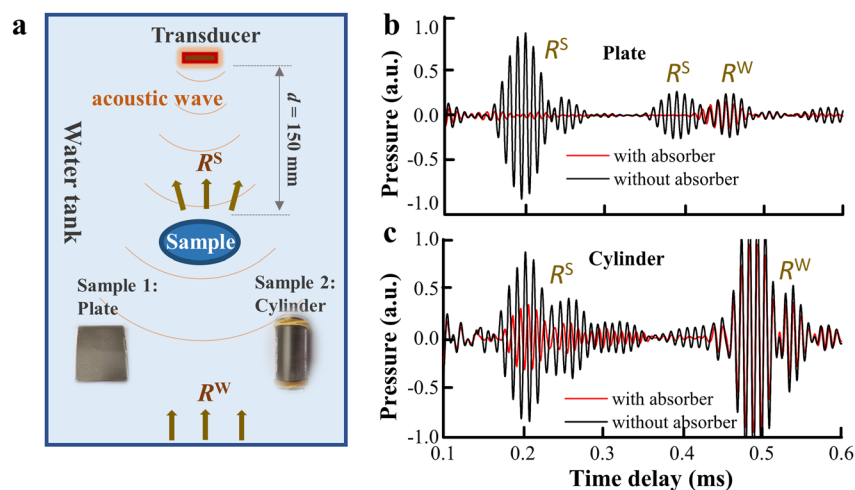


Fig. 5 Measurement of the acoustic stealth property at 100 kHz. **a** Schematic of the experimental setup for acoustic measurement in a water tank. A transducer will launch longitudinal acoustic waves and receive the reflected waves. The distance from the transducer to the sample is set to 150 mm. The operation frequency is 100 kHz, depending on the choice of emitter. The inset presents pictures of two samples: Sample 1—plate (left) and Sample 2—cylinder (right). **b, c** The measured time-trace ultrasonic signal for the plate and cylinder sample, respectively, with (red) and without the absorber (black). R^S and R^W represent the reflections from the sample and tank wall, respectively, as indicated in **a**.

(sample 1), with a nearly zero reflection in the back-and-forth traveling process. Note that a round transducer with a diameter of 38 mm is used here, which means that a spherical wave rather than a planar wave is excited. The measured result confirms the wide angular working performance of our AMS-based acoustic absorber, as theoretically predicted in Fig. 3c. The stealth function of our ultrathin acoustic absorber is then experimentally verified. When the same coat covers a brass cylinder (Sample 2), as shown in Fig. 5c, the acoustic returning loss from the cylinder is also largely reduced at an average reflectivity of $\sim 50\%$. The result basically agrees with the expectations derived from the angular absorption properties of the flat acoustic absorber. The side scattering from the edges of the cylinder would make reflections. However, considering the practical scenario where the probing distance is usually kilometers away, the side scattering for a single-station detection system may not be as serious, as the absorber is mostly explored for normal incidence. On the other hand, there will be techniques to broaden the angular response just like their EM counterparts^{44–46}.

Discussion

The multilayer ultrathin design proposed herein allows the optimization of the magnetic and acoustic properties individually, and more importantly, offers the freedom to integrate more functional substructures. For example, an active and acoustically transparent current boundary may be introduced, so that the magnetic cloak could cover a broader-frequency range, particularly for $f < 1$ kHz²⁰. For the acoustic part, we measured the acoustic stealth property at frequencies close to ~ 100 kHz. The bandwidth

could be improved by engineering the bubble shapes or their arrangement, for example, by an AMS consisting of a compound unit cell that has multiple fundamental resonances (see Supplementary Fig. S2a, b). In principle, the angular absorption property could also be improved with a gradient impedance design, such as an acoustic omnidirectional perfect absorber made of spatially dispersed Kramer–Kronig media⁴⁷ or acoustic “blackhole”^{48–50}. Like the EM designs, the AMS design could be proportionally rescaled so that the working-frequency band may be redshifted to kilohertz or lower frequencies for anti-sonar detection, or blueshifted to the ultrasonic spectrum for medical usage. For the latter, the combination with a magnetic cloak will vastly broaden the functionality, for example, enabling background field scattering to be controlled in nuclear magnetic resonance (NMR) imaging.

Last, it is necessary to emphasize that the relative position of the magnetic and acoustic layers in the biphysical coat is not fixed, and can be switched if both layers are thin enough, i.e., transparent to facilitate each other’s properties, which is particularly helpful for high-frequency applications. To demonstrate this point, as shown in Fig. 6a, we fabricate another sample consisting of brass ground, AMS, and FM layers from bottom to top. This experiment is also intentionally designed to inspect the application potential of the magnetic–acoustic dual-invisible coat for medical science by selecting MHz ultrasonic frequencies. After numerical optimization, the parameters for the air cavities in the AMS that we obtain are height $H = 36$ μm , diameter $D = 20$ μm , period $p = 210$ μm , and distance to the ground $d = 60$ μm . The

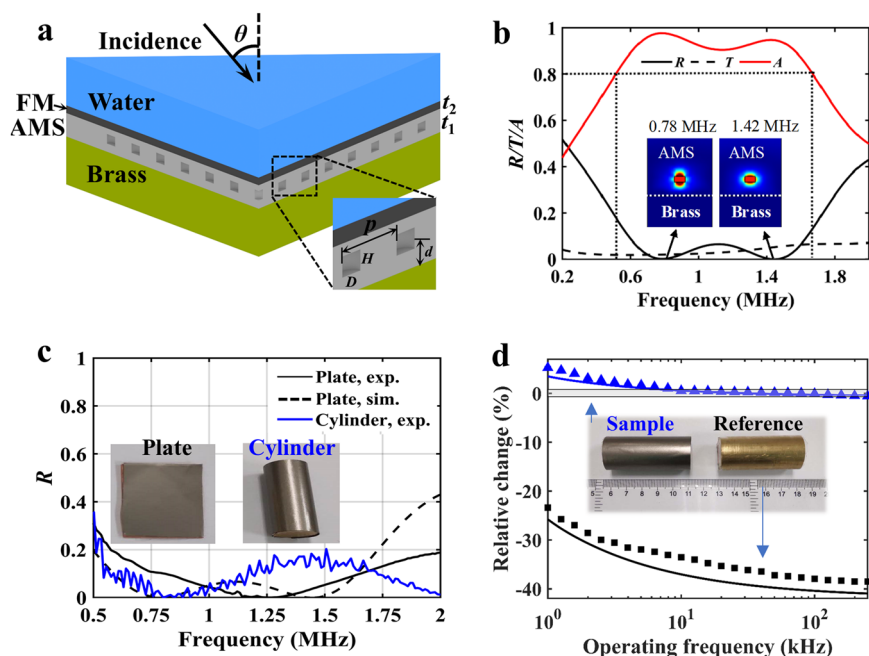


Fig. 6 Biphysical invisible coat operating at ultrasonic frequencies. **a** Schematic of the magnetic–acoustic dual-invisible coat. From top to bottom, it consists of an FM layer, an AMS layer, and a rigid brass ground. The AMS layer is made of a PDMS elastic sheet periodically doped with air-hole cavities. **b** The reflectance, transmittance, and absorbance spectra of the biphysical coat designed by the parameters $H = 36 \mu\text{m}$, $D = 20 \mu\text{m}$, $p = 210 \mu\text{m}$, $d = 60 \mu\text{m}$, $t_1 = 290 \mu\text{m}$, and $t_2 = 130 \mu\text{m}$. The inset draws the acoustic displacement in PDMS and pressure in the cavity at resonance frequencies of 0.78 and 1.42 MHz, respectively. **c** The measured reflectance spectra of the plate and cylinder samples. The solid lines are measured, and the dashed line is numerically calculated. The spectra are obtained from the Fourier transform of the measured time-domain pulse signal. **d** The measured relative change in the magnetic field at the point $(0, r_3 + 6 \text{ mm})$ caused by the sample and the reference as a function of the operating frequency. The inset presents pictures of these two samples.

thicknesses of the AMS and FM layers are $t_1 = 290 \mu\text{m}$ and $t_2 = 130 \mu\text{m}$, respectively (i.e., the total thickness of the biphysical coat is 0.42 mm). As shown in Fig. 6b, this sample numerically has a broadband acoustic absorption from 0.52 to 1.67 MHz, contributed by the two fundamental resonance modes (inset in Fig. 6b) occurring at 0.78 and 1.42 MHz, respectively, arising from the anisotropic shape ($D \neq H$) of the bubble cavity. The sample also has wide angular response properties (see Supplementary Fig. S3c–f). Figure 6c gives the measured reflectance spectra for a plate and a cylinder sample. The FM sheet and the brass cylinder have the same parameters as those used in the above experiment, which is reasonable because the ultrathin AMS could be practically neglected in the quasi-static approximation. For the plate sample, experimentally, we obtain a minimum reflectance ($R \rightarrow 0$) at 1.26 MHz and $R < 20\%$ at 0.58–2 MHz. A similar broadband performance is achieved for the cylinder sample. It is understood that the acoustic absorber will behave well at long probing distances when we compare the results with those shown in Fig. 5b, c. The measurement indicates that our sample has good magnetic cloaking behavior from 12.5 to 200 kHz, where $|\eta_H| < 0.5\%$ (Fig. 6d) (the bandwidth is slightly scarified

compared with that shown in Fig. 5c), and the phase variation is less than 1° (see Supplementary Fig. S4a, b). The maximum near-field field disturbance ratio for the 22-mm-thick brass cylinder is reduced by more than two orders of magnitude and 5 times in phase at the designed band (see Supplementary Fig. S4c, d). Therefore, it can be concluded that the ultrathin FM sheet can be robustly assembled with the properly designed AMS layer to induce biphysical invisible effects for various acoustic spectrum regimes.

In conclusion, we have proposed and demonstrated an artificial biphysical protecting ultrathin coat that can simultaneously deal with the detection of magnetic fields and acoustic waves for underwater objects. In principle, the compound design algorithm could be extended to render a 3D biphysical coat. For the future, the acoustic stealth performance could be further enhanced by graded AMS designs, which are particularly important for objects with irregular topologies. It is also possible to pattern the FM sheet with holes in order to make a single-layer magnetic–acoustic biphysical invisible coat. Regarding the applications, in addition to military purposes, we can imagine that this magnetic–acoustic bifunctional thin coat may find important uses in medical fields, for

example, to reduce magnetic and acoustic disturbances of implemented intrusions in a medical scan. Following the same idea, other functionalities or multiphysical systems may also be envisioned for waterborne science or technologies.

Acknowledgements

We are grateful to the partial support from NSFC (No. 61775195), NSFC of Zhejiang Province (Nos. LR15F050001 and LZ17A040001), and the National Key Research and Development Program of China (No. 2017YFA0205700).

Author details

¹State Key Lab of Modern Optical Instrumentation, Centre for Optical and Electromagnetic Research, College of Optical Science and Engineering, International Research Center for Advanced Photonics, Zhejiang University, 310058 Hangzhou, China. ²State Key Lab of Fluid Power and Mechatronic Systems, School of Mechanical Engineering, Zhejiang University, 310027 Hangzhou, China. ³School of Mechanical and Aerospace Engineering, Nanyang Technological University, Singapore 639798, Singapore. ⁴Centre for Optical and Electromagnetic Research, Guangdong Provincial Key Laboratory of Optical Information Materials and Technology, South China Academy of Advanced Optoelectronics, South China Normal University, Higher-Education Mega-Center, Guangzhou 510631, China

Author contributions

Y.Z. conducted most of the experiments and theoretical work. J.C. and Z.F. conducted part of the acoustic experiment. L.L. participated in the sample fabrication. Y.M. supervised the work. All the authors participated in the writing of the paper.

Conflict of interest

The authors declare that they have no conflict of interest.

Publisher's note

Springer Nature remains neutral with regard to jurisdictional claims in published maps and institutional affiliations.

Supplementary information is available for this paper at <https://doi.org/10.1038/s41427-020-0209-8>.

Received: 7 December 2019 Revised: 10 January 2020 Accepted: 16 January 2020.

Published online: 27 March 2020

References

- Pendry, J. B., Schurig, D. & Smith, D. R. Controlling electromagnetic fields. *Science* **312**, 1780 (2006).
- Leonhardt, U. Optical conformal mapping. *Science* **312**, 1777–1780 (2006).
- Schurig, D. et al. Metamaterial electromagnetic cloak at microwave frequencies. *Science* **314**, 977–980 (2006).
- Cai, W., Chettiar, U. K., Kildishev, A. V. & Shalae, V. M. Optical cloaking metamaterials. *Nat. Photon.* **1**, 224–227 (2007).
- Chen, H., Chan, C. T. & Sheng, P. Transformation optics and metamaterials. *Nat. Mater.* **9**, 387–396 (2010).
- Li, J. & Pendry, J. B. Hiding under the carpet: a new strategy for cloaking. *Phys. Rev. Lett.* **101**, 203901 (2008).
- Ergin, T., Stenger, N., Brenner, P., Pendry, J. B. & Wegener, M. Three-dimensional invisibility cloak at optical wavelengths. *Science* **328**, 337–339 (2010).
- Liu, R. et al. Broadband ground-plane cloak. *Science* **323**, 366–369 (2009).
- Ma, Y. et al. First experimental demonstration of an isotropic electromagnetic cloak with strict conformal mapping. *Sci. Rep.* **3**, 2182 (2013).
- Ma, H. F. & Cui, T. J. Three-dimensional broadband and broad-angle transformation-optics lens. *Nat. Commun.* **1**, 124 (2010).
- Urzhumov, Y. A. & Smith, D. R. Fluid flow control with transformation media. *Phys. Rev. Lett.* **107**, 074501 (2011).
- Greenleaf, A., Kurylev, Y., Lassas, M., Leonhardt, U. & Uhlmann, G. Cloaked electromagnetic, acoustic, and quantum amplifiers via transformation optics. *Proc. Natl Acad. Sci. USA* **109**, 10169–10174 (2012).
- Zhang, S., Genov, D. A., Sun, C. & Zhang, X. Cloaking of matter waves. *Phys. Rev. Lett.* **100**, 123002 (2008).
- Ma, Y., Liu, Y., Raza, M., Wang, Y. & He, S. Experimental demonstration of a multiphysics cloak: manipulating heat flux and electric current simultaneously. *Phys. Rev. Lett.* **113**, 205501 (2014).
- Gömöry, F. et al. Experimental realization of a magnetic cloak. *Science* **335**, 1466–1468 (2012).
- Souc, J. et al. A quasistatic magnetic cloak. *New J. Phys.* **15**, 053019 (2013).
- Solovoyov, M., Souc, J. & Gömöry, F. Magnetic cloak for low frequency AC magnetic field. *IEEE Trans. Appl. Supercond.* **25**, 1–5 (2015).
- Zhu, J. et al. Three-dimensional magnetic cloak working from d.c. to 250 kHz. *Nat. Commun.* **6**, 8931 (2015).
- Jiang, W. et al. Room-temperature broadband quasistatic magnetic cloak. *NPG Asia Mater.* **9**, e341 (2017).
- Jiang, W., Ma, Y. & He, S. Static magnetic cloak without a superconductor. *Phys. Rev. Appl.* **9**, 054041 (2018).
- Chen, H. & Chan, C. T. Acoustic cloaking in three dimensions using acoustic metamaterials. *Appl. Phys. Lett.* **91**, 183518 (2007).
- Cummer, S. A. et al. Scattering theory derivation of a 3D acoustic cloaking shell. *Phys. Rev. Lett.* **100**, 024301 (2008).
- Torrent, D. & Sánchez-Dehesa, J. Anisotropic mass density by radially periodic fluid structures. *Phys. Rev. Lett.* **105**, 174301 (2010).
- Zhang, S., Xia, C. & Fang, N. Broadband acoustic cloak for ultrasound waves. *Phys. Rev. Lett.* **106**, 024301 (2011).
- Popa, B.-I., Zigoneanu, L. & Cummer, S. A. Experimental acoustic ground cloak in air. *Phys. Rev. Lett.* **106**, 253901 (2011).
- Zigoneanu, L., Popa, B.-I. & Cummer, S. A. Three-dimensional broadband omnidirectional acoustic ground cloak. *Nat. Mater.* **13**, 352 (2014).
- Bi, Y., Jia, H., Lu, W., Ji, P. & Yang, J. Design and demonstration of an underwater acoustic carpet cloak. *Sci. Rep.* **7**, 705 (2017).
- Chen, Y. et al. Broadband solid cloak for underwater acoustics. *Phys. Rev. B* **95**, 180104 (2017).
- Bückmann, T., Thiel, M., Kadic, M., Schittny, R. & Wegener, M. An elasto-mechanical unfeelability cloak made of pentamode metamaterials. *Nat. Commun.* **5**, 4130 (2014).
- Ivansson, S. M. Numerical design of alberich anechoic coatings with superellipsoidal cavities of mixed sizes. *J. Acoust. Soc. Am.* **124**, 1974–1984 (2008).
- Zhang, C. et al. Multiphysical digital coding metamaterials for independent control of broadband electromagnetic and acoustic waves with a large variety of functions. *ACS Appl. Mater. Interfaces* **11**, 17050–17055 (2019).
- Bai, G. D. et al. Manipulation of electromagnetic and acoustic wave behaviors via shared digital coding metallic metasurfaces. *Adv. Intell. Syst.* **1**, 1900038 (2019).
- Munk, B. A., Munk, P. & Pryor, J. On designing jaumann and circuit analog absorbers (CA absorbers) for oblique angle of incidence. *IEEE Trans. Antennas Propag.* **55**, 186–193 (2007).
- Zhong, S. et al. Transparent transmission-selective radar-infrared bi-stealth structure. *Opt. Express* **26**, 16466–16476 (2018).
- Leroy, V. et al. Superabsorption of acoustic waves with bubble metascreens. *Phys. Rev. B* **91**, 020301 (2015).
- Yang, M., Chen, S., Fu, C. & Sheng, P. Optimal sound-absorbing structures. *Mater. Horiz.* **4**, 673–680 (2017).
- Huang, Z. et al. A General patterning approach by manipulating the evolution of two-dimensional liquid foams. *Nat. Commun.* **8**, 14110 (2017).
- Prat-Camps, J., Navau, C. & Sanchez, A. A magnetic wormhole. *Sci. Rep.* **5**, 12488 (2015).
- Leroy, V. et al. Design and characterization of bubble phononic crystals. *Appl. Phys. Lett.* **95**, 171904 (2009).
- Leroy, V., Strybulevych, A., Page, J. H. & Scanlon, M. G. Influence of positional correlations on the propagation of waves in a complex medium with poly-disperse resonant scatterers. *Phys. Rev. E* **83**, 046605 (2011).
- Calvo, D. C., Thangawng, A. L. & Layman, C. N. Low-frequency resonance of an oblate spheroidal cavity in a soft elastic medium. *J. Acoust. Soc. Am.* **132**, EL1–EL7 (2012).
- Meng, H., Wen, J., Zhao, H., Lv, L. & Wen, X. Analysis of absorption performances of anechoic layers with steel plate backing. *J. Acoust. Soc. Am.* **132**, 69–75 (2012).

43. Leroy, V., Strybulevych, A., Scanlon, M. G. & Page, J. H. Transmission of ultrasound through a single layer of bubbles. *Eur. Phys. J. E* **29**, 123–130 (2009).
44. Zhu, J. et al. Ultra-broadband terahertz metamaterial absorber. *Appl. Phys. Lett.* **105**, 021102 (2014).
45. Zhou, Z. et al. Metasurface salisbury screen: achieving ultra-wideband microwave absorption. *Opt. Express* **25**, 30241–30252 (2017).
46. Tao, H. et al. Highly flexible wide angle of incidence terahertz metamaterial absorber: design, fabrication, and characterization. *Phys. Rev. B* **78**, 241103 (2008).
47. Jiang, W. et al. Deformable broadband metamaterial absorbers engineered with an analytical spatial kramers-kronig permittivity profile. *Laser Photon. Rev* **11**, 1600253 (2017).
48. Naify, C. J. et al. Underwater acoustic omnidirectional absorber. *Appl. Phys. Lett.* **104**, 073505 (2014).
49. Narimanov, E. E. & Kildishev, A. V. Optical black hole: broadband omnidirectional light absorber. *Appl. Phys. Lett.* **95**, 041106 (2009).
50. Yang, Y., Leng, L. Y., Wang, N., Ma, Y. & Ong, C. K. Electromagnetic field attractor made of gradient index metamaterials. *J. Opt. Soc. Am. A* **29**, 473–475 (2012).